Available online at www.sciencedirect.com
SCIENCE DIRECT®
PERGAMON
International Journal of Heat and Mass Transfer 46 (2003) 1703–1713
International Journal of HEAT and MASS TRANSFER
www.elsevier.com/locate/ijhmt

Simultaneous visualization of flow field and evaluation of local heat transfer by transitional impinging jets

M. Angioletti [a], R.M. Di Tommaso [a], E. Nino [a], G. Ruocco [b,*]

[a] DIFA, Università degli Studi della Basilicata, Campus Macchia Romana, 85100 Potenza, Italy
[b] DITEC, Università degli Studi della Basilicata, Campus Macchia Romana, 85100 Potenza, Italy

Received 6 February 2002; received in revised form 25 November 2002

Abstract

A combined approach has been employed to characterize the flow field and local heat transfer in jet impingement configurations, featuring a mass transfer experiment and a digital visualization technique. A jet velocity range is spanned to ensure flow regime transition.

The well-known heat/mass transfer analogy has been used to infer on the local heat exchange on a infinite plate. In this experiment, a naphthalene film is ablated from a disk, due to jet exposure. Automated contact measurements of the variation of film depth in the stagnation region and beyond have been performed. From the local naphthalene loss rate the local heat transfer is then inferred. Coherent structures are created both at the interface between free jet and quiescent medium and upon impingement at plate, and need to be visualized in the vicinity of stagnation. To this end a particle image velocimetry system is exploited to extract the two components velocity instantaneous information.

Ablation measurements confirm the non-monotonic progress of local heat transfer for small nozzle-to-plate spacings. The visualizations evidence that local heat transfer is strongly influenced by impingement structures: the maximum heat transfer coefficient offset which can be detected is due, even for laminar or transitional jet, to large-scale toroidal vortices impacting on the plate.

Keywords: Jet impingement; Local heat transfer; PIV visualization; Mass transfer analogy

1. Introduction

Jet impingement (JI) exhibits very favorable local and controlled mass and heat transfer characteristics. This well-known technique consists in directing a jet flow from a nozzle of a given configuration to a target surface. For a planar, unconfined configuration (impinging on an indefinite plate) the flow structure can be summarized into three characteristic regions, shown in Fig. 1: the free jet region formed as jet exits with a $V(r)$ velocity distribution, the impingement (stagnation) flow region formed upon jet impact and deflection, and the wall jet region formed upon re-acceleration of the flow along the confining surface. Large transfer coefficients are attainable in the vicinity of the stagnation region, but a portion of the wall jet region may significantly contribute to the heat exchange. JI studies are sustained by a considerable interest due to their potential application in industrial thermal control and material conditioning and processing. The drying of textiles, paper or film material, the annealing of metal or plastic sheets, the tempering of glass, the cooling of gas turbine blades and the micro-scale heat transfer are but a few of their important practical implementation.

A large literature set is available on gaseous JI, as it has been extensively characterized the past five decades. Yet, most studies have been mainly concerned with turbulent jets (for example, as found by the most recent reviews [1,2]), but it has to be considered that the

* Corresponding author.
E-mail addresses: nino@unibas.it (E. Nino), ruocco@unibas.it (G. Ruocco).

0017-9310/03/$ - see front matter
doi:10.1016/S0017-9310(02)00479-9

Nomenclature

d	nozzle diameter, m	Pr	Prandtl number
D	naphthalene–air diffusion coefficient, m^2/s	Re	Reynolds number, based on nozzle diameter
ϵ	error in the mass transfer experiments	ρ_s	density of solid naphthalene, kg/m^3
h	nozzle–plate distance (nozzle height), m	ρ_v	naphthalene vapor density at impingement surface, kg/m^3
h_m	mass transfer coefficient, m/s, Eq. (1)		
Nu	Nusselt number	Sc	Schmidt number, Eq. (3)
Nu_0	Nusselt number at stagnation	Sh	Sherwood number, Eq. (2)
Nu_{max}	maximum Nusselt number	V	air velocity, m/s
v	kinematic viscosity of air, m^2/s	V_{av}	average air velocity at nozzle exit, m/s

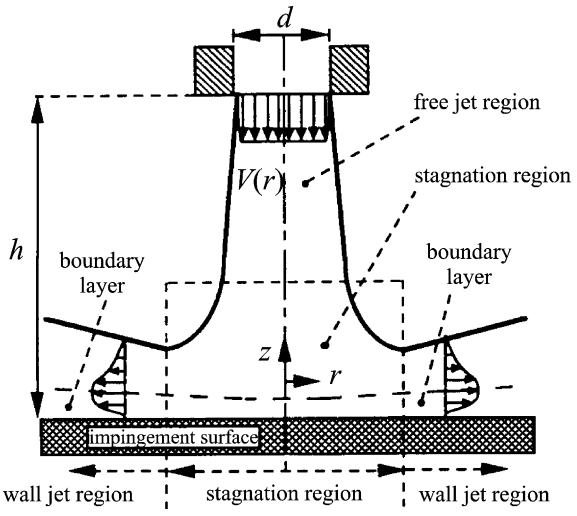

Fig. 1. Flow regions for an impinging free-surface jet.

exchange characteristics are favorable even for low volumetric flows (as for electronic components cooling in portable applications [3]), initially in laminar regime or undergoing transition, when the nozzle-to-plate spacing is small and a large stagnation pressure is not desirable. The exploitation of such configuration brings over the motivation for the present work. The limit at which the circular non-confined jet becomes a transition or semi-turbulent one is for $Re = 1000$ [2], based on nozzle diameter; particularly, the present work focuses on local heat transfer to a single non-confined, impinging round jet, leaving the nozzle with a uniform profile, in the 1000–4000 range and moderately close to the target surface. In the literature review that follows, those papers which do not pertain to round, gaseous unconfined JI are kept aside as they form a different literature set: as an example, the complete range of fluid dynamics regimes ($700 \leqslant Re \leqslant 7000$) explored by Elison and Webb [4], cannot be taken into consideration for the present context as their results are relative to liquid JI.

A pioneer report on local heat transfer in circular air jet has been provided by Gardon and Akfirat [5], but for a minimum $Re = 2500$ and an otherwise unspecified submerged arrangement. Similar approaches have been performed by Vickers [6] for Re in the 250–950 range, with Re/jet height combinations of little use in this context (minimum $h/d = 4.9$ for maximum $Re = 550$), and by Huang [7] who confined his study to the stagnation point (i.e., under the jet centerline) for highly turbulent regimes, but their pertinence has been further limited as the adopted nozzle geometries and related initial jet shape $V(r)$ remained undescribed.

A theoretical and experimental investigation on mass transfer was then performed by Scholtz and Trass [8] for a wide range of nozzle-to-plate spacings and $500 \leqslant Re \leqslant 1960$, but their experimental findings were characterized by non-uniform profile shape at the nozzle exit, and only limited reference was made to mass transfer beyond the stagnation region in the transition regime ($Re = 1000$). However, this work evidenced that the mass transfer coefficient differs significantly depending on the jet shape, as non-uniform profiles lead to altered results compared to theoretical uniform ones, specially in the stagnation region. The importance of the jet shape was numerically confirmed few years later by Saad et al. [9] for a semi-confined round air jet. Local heat transfer measurements were carried out by Sparrow and Lovell [10] for initially laminar JI for circular nozzles, for several nozzle–surface separations under a variety of inclination angles including the normal, but limited to a still turbulent flow regime (minimum $Re = 5000$ for reported local heat transfer).

As reported in [1,2], JI assessment has also been performed by exploiting various heat and mass transfer principles, e.g. *trans*-cinnamic acid surfaces impinged by water, electrolytic transfer, calorimetry, infrared imaging, liquid crystals, and moisture transfer from impinged porous plates. A further, well-established mass transfer technique, the sublimation of naphthalene, was used in JI by Sparrow and Lovell [10], and with confidence in a variety of other convective heat transfer applications.

One may refer for completeness to the review by Goldstein and Cho [11], or to the preliminary work by Angioletti et al. [12] for a JI configuration similar to the present one.

Useful inferences were brought over by flow field visualization. A detailed, high-resolution flow visualization for a confined, round JI has been first presented by Yokobori et al. [13] using a hydrogen bubble technique, then Popiel and Trass [14] contributed for similar configuration by employing the smoke–wire visualization. However, both papers provided a qualitative description only of the resulting flow field. Then, Anderson and Longmire [15] characterized a particle-laden JI by laser illumination and particle image velocimetry (PIV), but for Re larger than 2×10^4, while Sakakibara et al. [16] presented coupled velocity–temperature profiles for plane water, limited to a minimum Re as low as 2000.

This exploration of the available literature clearly shows that a further physical insight into the near-field of initially uniform and laminar, gaseous round impinging jets is needed, as this fluid–solid interaction is still complex even at low volumetric rates. Typical local heat transfer progress has to be confirmed for an initially laminar regime and its coupling with the flow field characteristic behavior has to be explained. To this end, a combined approach is taken, featuring a flow visualization technique and the mass transfer analogy.

2. Measurements and visualization techniques

2.1. Mass transfer measurement and data reduction procedure

A heat transfer measurement carried out by the naphthalene sublimation method, based on the heat/mass transfer analogy, has the main advantage of excluding large wall-conduction errors resulting from steep gradients in the transfer rates across the region of interest. Acceptable accuracies are possible, in general, even with low-velocity flows when thermal control is ensured, since the vapor pressure of naphthalene varies by about 10% per K at room temperature [11]. The shape change of the region of interest can also be neglected with the configuration at hand, as the ablated depth is relatively shallow and there is no influence on the flow field. In the reported measurements naphthalene plates have been ablated by exposure to JI within a large controlled ventilation chamber (CVC), otherwise employed in industrial ventilation studies, allowing to set and keep the internal surfaces to a given temperature.

The active mass transfer region, the naphthalene test plate, is produced by melting some purified naphthalene in a double boiler at 361 K. The test plate is framed by a coplanar hollow stainless steel plate, which is formed by two coupled halves. The overall dimension of the impingement surface is 200 mm × 200 mm with 19-mm thickness, with a 100-mm hole. The hollow frame, when joined to a base plate which has been lapped and polished in order to yield a mirror-like finish, realizes a mold cavity that is appropriately heated to eliminate any temperature gradient upon pouring of the molten naphthalene. Once the complete solidification is attained, the base plate can be detached from the test frame thereby yielding a cast naphthalene surface that possesses the required smoothness and flatness. The cast and its steel frame are then placed in the CVC to attain thermal equilibrium. During this period, the test surface is covered with an impermeable film to prevent sublimation by natural convection.

The layout of the simple JI system is reported in Fig. 2a. Air is drawn from the outdoor and stored in an adiabatic compressor plenum (not shown), from which it is ducted through a flow meter to a hose ending with a smaller secondary plenum of approximately 1×10^{-2} m^3. The regularity of the airflow has been ensured by a regulating valve and carefully checked throughout the tests. The air temperature at the exit has also been monitored by a thermocouple. The secondary plenum is suspended above the test plate by a micrometer static guide, and is levelled as normal with respect to the impinged plate. The air is then blown through an attached 10-mm TSI calibrated converging nozzle, which ensures an essentially uniform initial velocity profile $V(r) = V_{av}$ and low turbulence, and impinges on the naphthalene test plate. Stale air is then withdrawn by a CVC blower and ducted to an exhaust and to the outdoor. After the ablation, to perform the measurements of the local variation of film ablation in the stagnation region and beyond, the test surface is placed on a micrometer driven, 2-axes translation custom-made stage (Fig. 2b), featuring a travel range of 400 mm and a resolution of 0.1 mm. In this set of measurements, a lateral displacement of 0.5 mm has been enforced. The translation stage carries a micrometric contact sensor, based on resistance difference due to position variation, which is translated into linear voltage representation of the travelled depth. The sensor measurement range is 3.5 mm. The signal is acquired by an I/O board (Advantech PCL 818 HG), and the sensor acquiring system has an uncertainty of ± 0.01 mm. An in-house software deals with translation/measurement synchronization.

To avoid any influence on extraneous mass transfer, due to natural convection or other spurious air drafts, measurements of the local surface elevation of the naphthalene plate have been made both before and after an ablation run, in a timely fashion. In order to seek the closure of the mass balance, the test plate is removed from the detachable frame and weighted before and after each test run with an analytical balance which discriminates down to 0.01 mg. Typically, the mass variation during a run is in the 100–300 mg range, and

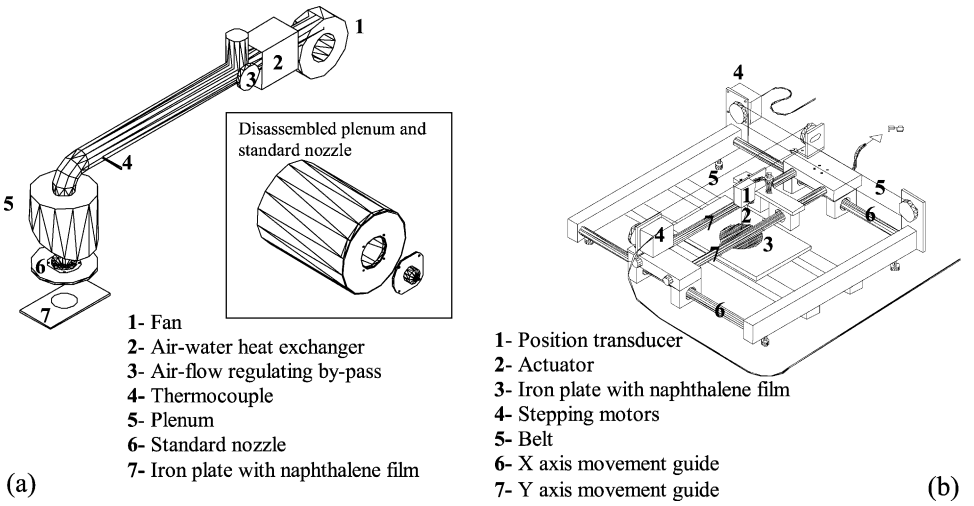

Fig. 2. JI set-up and components for (a) ablation and (b) measurement.

agreement between numerical integration of local transfer coefficient over the plate surface and the weighing procedure is within 10%.

A local mass transfer coefficient h_m can be defined as

$$h_m(r) = \frac{\rho_s \Delta z(r)}{\rho_v \Delta \tau} \tag{1}$$

where ρ_s is the density of solid naphthalene (equal to 1.145×10^3 kg/m^3), ρ_v is the naphthalene vapor density at the impingement surface, $\Delta z(r)$ is the net sublimation local depth, and $\Delta\tau$ is the total exposure time under the jet flow.

Total naphthalene sublimation depth is calculated from the change in measured surface elevations before and after the exposure. The net sublimation depth was generally 0.2–1.8 mm in the entire ablated region, the maximum depth being detected in the stagnation region. The empirical equation of Ambrose et al. [17] is used to determine the naphthalene vapor pressure; from the ideal gas law, naphthalene vapor density on the surface is then computed. The results can be expressed in terms of the dimensionless counterpart of the local mass transfer coefficient, the Sherwood number

$$Sh(r) = \frac{h_m(r) d}{D} \tag{2}$$

Numerical values for the naphthalene–air diffusion coefficient D were obtained from the kinematic viscosity of air v and the following defining equation of the Schmidt number:

$$Sc = \frac{v}{D} \tag{3}$$

which is 2.28 for the naphthalene–air system. The results can be parameterized by the dimensionless separation distance h/d and the customary Re, already alluded to.

A heat transfer perspective can then be gained, by invoking the aforementioned analogy between heat and mass transfer. According to this, the conversion between the Sh and Nusselt numbers results, at a given Re, can be accomplished by the following relation [11]:

$$Nu(r) = \left(\frac{Pr}{Sc}\right)^{0.4} Sh(r) \tag{4}$$

This analogy requires that the boundary conditions for the two processes be analogous. Thus, the uniform wall concentration (i.e., ρ_v = constant) of the present experiment translates into uniform wall temperature for the heat transfer case.

The uncertainty on Nusselt number results depends on temperature and ablation depth measurements. The influence of temperature measurements (uncertainty of ± 0.5 K at 283.15 K) influences the naphthalene vapor pressure determination and then the Nusselt number with a percentile error ϵ_T of 0.8%. Ablation depth measurements are affected by two kinds of error: measuring system uncertainty, and I/O board random errors. The sensor acquiring system uncertainty (± 0.01 mm) gives a local error ϵ_U on calculated Nusselt number of $0.28/Nu$; the random error of I/O board due to electrical noise can be determined performing measurements on a "cold" surface (with no sublimation). The mean value of the errors is less than 0.003 mm and the standard deviation σ of rms values is 0.02 mm. Therefore the random error is 0.04 mm (2σ) at a 95% confidence level and the consequent error ϵ_E on the local Nusselt is $0.95/Nu$. The total local error ϵ on the Nusselt distribution can be evaluated by a summation in quadrature:

$$\epsilon = \sqrt{\epsilon_T^2 + \epsilon_U^2 + \epsilon_E^2} \tag{5}$$

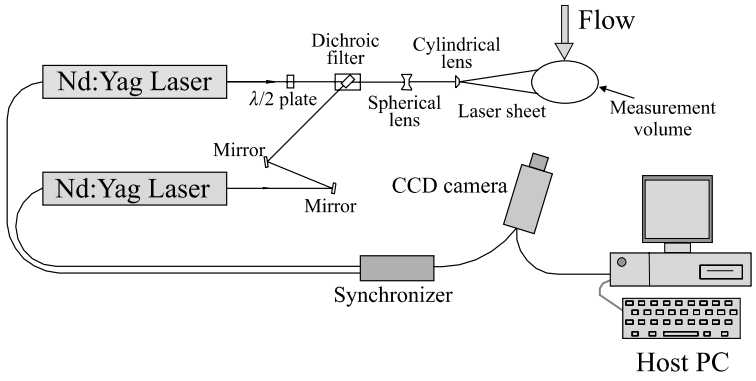

Fig. 3. PIV set-up and system components.

The evaluated local error ϵ values are in the range 3–20% and the related uncertainty $\epsilon \times Nu$ is in the range ($\pm$1.0)–($\pm$1.2).

2.2. Particle image velocimetry

A PIV system has been employed to analyze the instantaneous behavior of the velocity field. The adopted system (whose layout is reported in Fig. 3) is based on two pulsed Nd:YAG lasers firing on the second harmonic (green 532 nm). The beams, properly separated in time, are recombined on the same optical path by a polarized dichroic filter. Then the beams are expanded in one direction, by a combinations of spherical (negative) and cylindrical lens, to obtain a 100 mm wide and 0.3 mm thick laser sheet in the measuring region. The laser sheet is used to illuminate the airflow below the nozzle and over the plate. A fog generator has been used to disperse water droplets seeding in the feed duct to the test nozzle.

The images have been collected by of a double frame 1000×1000 pixels Kodak CCD camera synchronized with the two laser beams and with the frame grabber by means of a dedicated electronic synchronizer. The images are formed by two different layers, each of them containing information about the seeding positions obtained by firing one of the two lasers. So the initial seeding positions (first laser beam, image on the first layer) and the final one (second laser beam, image on the second layer) are spotted. This practice allowed to avoid the polarity ambiguity, which affects the standard PIV technique [18,19].

The images were then post-processed by means of the TSI Insight v.3.2 software in order to extract the sub-images formed by 32×32 pixels from each layer, and to perform a cross-correlation between the two corresponding sub-images. An interrogation algorithm extracts the correlation peak position from the cross-correlation domain with a sub-pixel precision, and performs the calculation of the two velocity components for those sub-images, by a pixel-to-mm conversion factor. Interrogations are repeated using a recursive algorithm for the entire set of double frames images. The measured velocities are reported in a grid with size of 32×32 pixels with a 50% overlap (Nyquist criteria), i.e., in a square grid with size ranging from 0.43×0.43 to 0.59×0.59 mm^2, depending on the explored geometric configuration (nozzle height and inclination where applicable). The two laser beams have been fired at about 100 mJ per pulse (second harmonic), and with separation time of 40 ms. The measurement volume has been stretched up to 1 mm from the impinged plate. The overall estimated error has been evaluated, according to [20,21], as about 4% on V_{av}.

3. Results and discussion

3.1. Preliminaries

A total of four different combinations of Re and h/d have been explored in the present work: Re ranges from 1000 to 4000, and two geometric configurations are used, h/d equal to 2 or 4.5 (Table 1). For all configurations, the exposure time was kept at 7.56×10^4 s, and temperature and pressure were carefully monitored as constant and respectively 298 K and 950 mbar. First, the nozzle flow geometry and uniformity had to be assessed, as a non-uniform initial jet distribution may determine up to a twofold value in the mass transfer features, both

Table 1
Explored configurations

Configuration number	h/d	Re
1	2.0	1000
2	2.0	4000
3	4.5	1500
4	4.5	4000

in the stagnation region and the wall jet region [8]. Therefore a preliminary visualization has been performed by a LDV system to confirm the uniformity of $V(r)$ from the employed calibrated nozzle.

3.2. Visualization of large-scale structures

A refined flow analysis has been carried out by performing PIV measurements on configuration 1. Fig. 4 focuses on the stagnation and wall jet regions. The instantaneous velocity field reveals that, even for the smallest Re and h/d values, vortices are created on the stagnation zone side. These entrain "fresh" fluid allowing for repeated interaction with the target surface starting on the side of the stagnation region, thus resulting in enhanced heat transfer. The occurrence of an attached wall flow is also depicted, though the vortices which separate from the stagnation region disperse starting at about 2.0 r/d, due to momentum loss. Pulsation of the jet core is barely present but stagnation is well formed at this fluid regime.

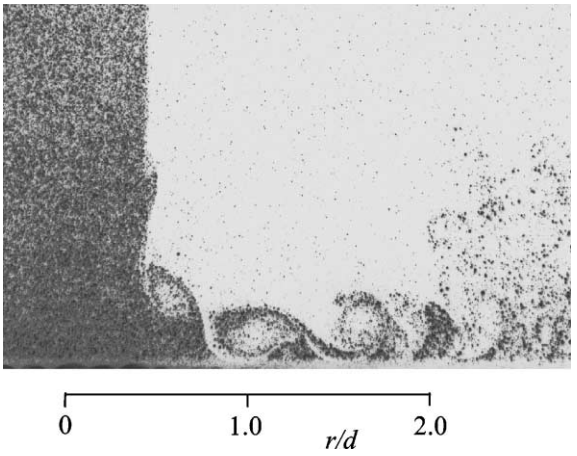

Fig. 4. Instantaneous velocity field in the stagnation and wall jet regions by PIV for configuration 1 ($h/d = 2.0$, $Re = 1000$).

The nature of the solid–fluid interaction can inspected further by displaying the entire flow field below the nozzle, and following the vortex deployment and related entrainment when a higher h/d value is adopted. This allows to study how the large-scale ordered flow structure of the JI affects the flow at the plate surface in the impingement region. Let us comment the flow field for the transitional configuration 3 (Fig. 5). If three images, from 1a to 3a, are recorded at a very short time interval, a sequence of discrete toroidal vortices can be seen that are created, along the interface between the jet and the surrounding air, and subsequently impinge on the plate. For sake of presentation, a reference vortex is initially identified, and marked along the entire progress to impingement: an almost perfect axial symmetry of the toroidal vortex pattern is found, as expected.

A related post-processed series of images is conveniently provided in Fig. 6. These vector representations are reported for each flow field from 1b to 3b. As the reference vortex approaches the plate it stretches, increasing its diameter. The normal velocity component tends to zero, so to conserve the momentum the radial component gets stronger, and a larger vortex reaches the plate. The impact region is slightly offset with respect the vertical, due to the action of the stagnation region.

At this regime, structures are visible that are rotating according to free jet flow and no counter-rotating structures are detected. In spite of vortices growth the jet core would not disappear therefore stagnation is still well formed underneath the jet and just slightly contracted within its diameter. The r/d distance at which the vortex reaches the plate is read as 0.7–0.9 from the jet axis, in accord with the smoke–wire pictures and

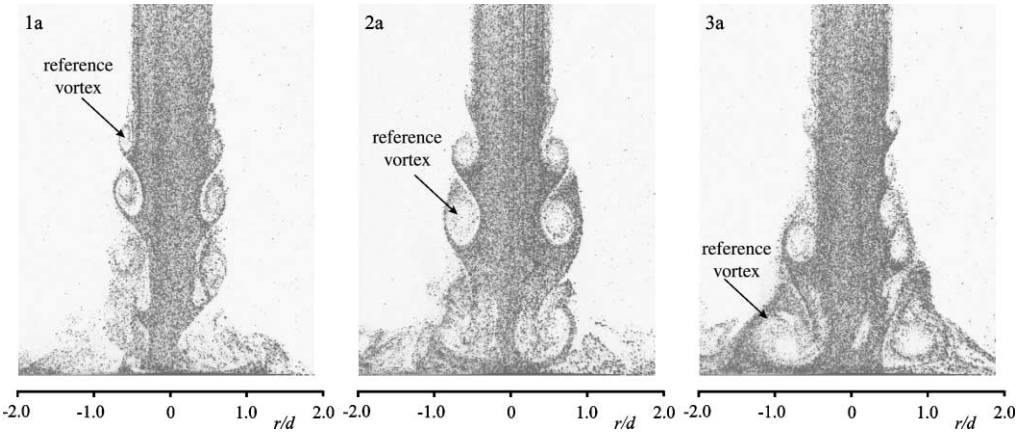

Fig. 5. A close-sequence of the three instantaneous flow fields (from 1a to 3a) below the nozzle by PIV for configuration 3 ($h/d = 4.5$, $Re = 1500$), with a marked reference vortex.

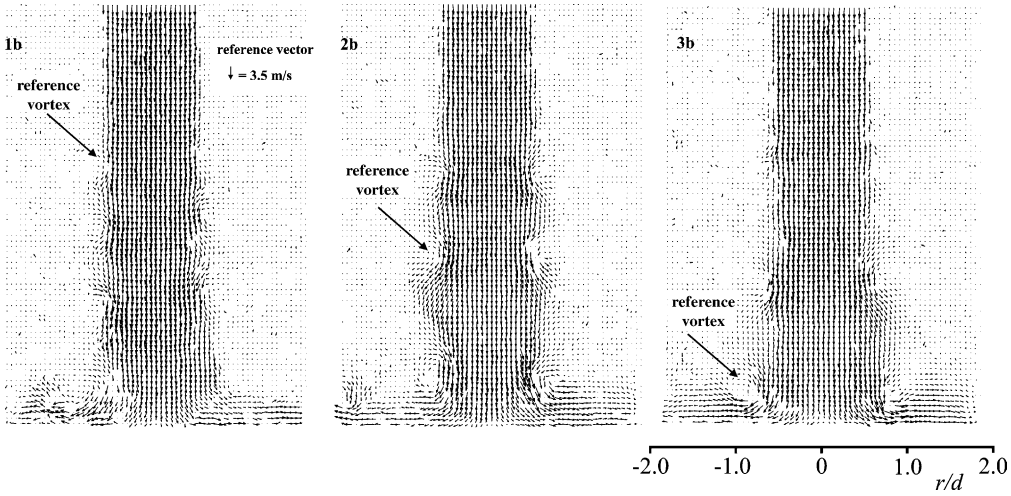

Fig. 6. Post-processed vector representations of configuration 3 ($h/d = 4.5$, $Re = 1500$), corresponding to images in Fig. 5.

assessment in [14], and with the PIV investigation in [15] although for much higher *Re*. This is the region where the large-scale toroidal structures interact with the impingement surface by destroying the stagnation boundary layer, and where large fluctuations of local skin friction (and heat and mass transfer) are therefore expected, as anticipated by Saad et al. [9] though for a higher $h/d = 8$. This inference also satisfies the unanswered question by Gardon and Akfirat [5] on which mechanism would produce a secondary heat transfer enhancement, regardless of the laminar or turbulent regime.

To further investigate on the large-scale structures pattern and implications, the quantitative PIV data are further post-processed, by subtracting the V_{av} across the entire displayed flow field, for a sample instantaneous picture for configuration 3. In Fig. 7 such result is reported, with the indications of different main regions. The potential core extends below the nozzle exit down to $h/d \approx 2.7$ and features a null vector field, i.e., the flow velocity is practically constant and equal to V_{av}; below it a deceleration region exists, evidenced by a reversed vector field, down to $h/d \approx 2.1$; then an acceleration region follows, down to $h/d \approx 1.0$, which is due to toroidal vortex growth. This region moves with the vortex, therefore the bulk flow beneath the nozzle pulsates axially due this vortex growth and translation. A last region is finally evident where the flow strongly decelerates as the effect of target surface is gradually felt.

The relative axial velocity magnitude can be then extracted along the jet axis and presented in Fig. 8, where the related PIV image is also provided, with indications of same regions reported in Fig. 7. A flow axial pulsation can be noticed, due to the vortices action, as the velocity magnitude fluctuates of more than ±40%, starting from the potential core. It must be taken into consideration that different instantaneous fields are characterized by different pulsation magnitudes and region locations, as the main vortex travels on its way to target impact.

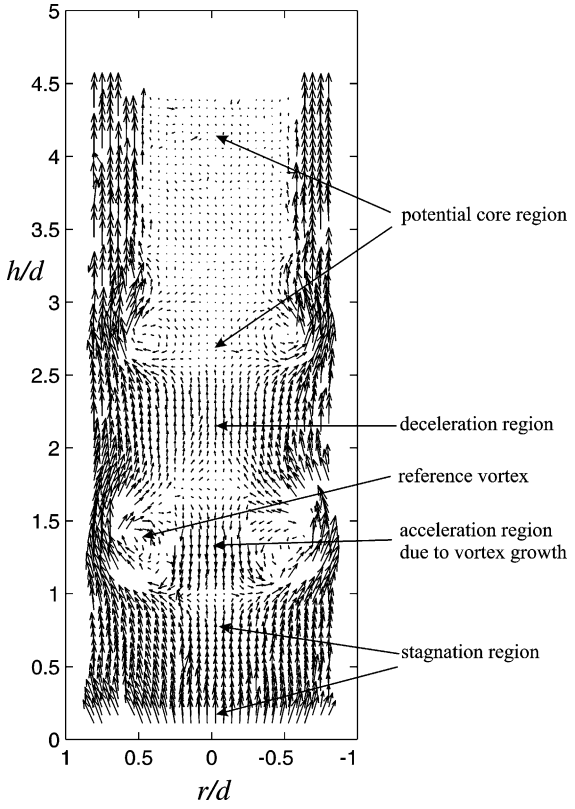

Fig. 7. PIV post-processed instantaneous flow field and characteristic region pattern for configurations 3 ($h/d = 4.5$, $Re = 1500$).

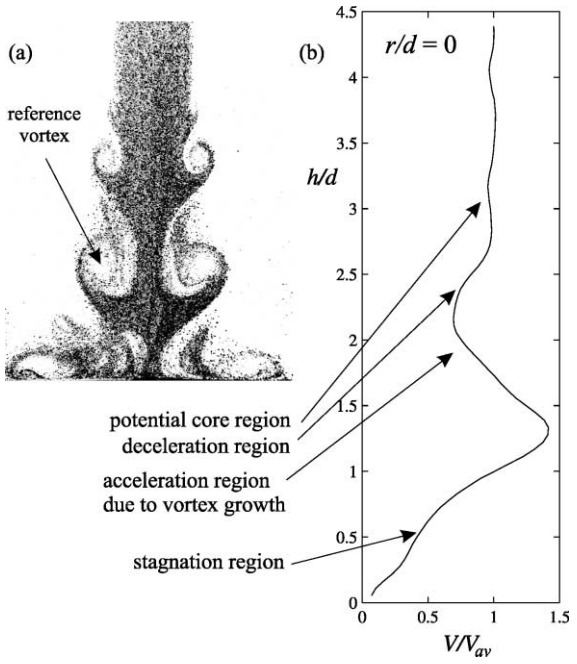

Fig. 8. PIV image with the reference vortex (a) and post-processed instantaneous axial velocity distribution $V = V(h/d)$ at $r/d = 0$ (b) for configurations 3 ($h/d = 4.5$, $Re = 1500$), with region pattern.

3.3. Flow field influence on local heat transfer

A first assessment of quantitative heat transfer can be performed by examining in Fig. 9 the $Nu(r/d)$ progress translation of the ablated naphthalene profile for configurations 3 and 4. The maximum Nusselt number Nu_{max} for configuration 3 is 44.73, detected at the offset $r/d = -0.3$, while the stagnation Nusselt number Nu_0 is 43.70 (Table 2). It can be inferred that this heat transfer augmentation offset is due to the impingement of the large-scale toroidal structure noticed in Figs. 5 and 6. The familiar bell shape is also observed, though changes of progress inclination are seen starting at $r/d \approx 1$ and $r/d \approx 2$, corresponding to opposite influences of mixing-induced turbulence and diminished velocity. For configuration 4 Nu_{max} (recorded at a negligible offset) and Nu_0 are respectively 51.50 and 51.36 (Table 2). The comparison shows the expected increase of heat transfer with Re; the absence of the saddle-effect and limited perturbations in the progress of heat transfer in the wall jet region, for higher Re, suggest a relative independence of turbulent JI on large-scale structures, for a relatively large nozzle-to-plate spacing.

Table 2
Summary of maximum and stagnation Nusselt number values, and related uncertainty, for the explored configurations

Configuration number	Nu_{max}	r/d	Nu_0
1	34.15 ± 1.11	−0.4	31.28 ± 1.10
2	52.48 ± 1.17	+0.4	49.27 ± 1.16
3	44.73 ± 1.14	−0.3	43.70 ± 1.14
4	51.50 ± 1.17	+0.1	51.36 ± 1.17

A second comparison is shown in Fig. 10 between configurations 1 and 2, suggesting that the increase of heat transfer with Re is comparatively larger for the shallow geometry ($h/d = 2.0$). For configuration 1 the absolute maximum $Nu_{max} = 34.15$ is again not detected at the nozzle axis, but at the largest offset $r/d = -0.4$, while Nu_0 is 31.28 (Table 2). Thus, the influence of aforementioned structures on the heat transfer enhancement is evident even at a lower (transitional) Re.

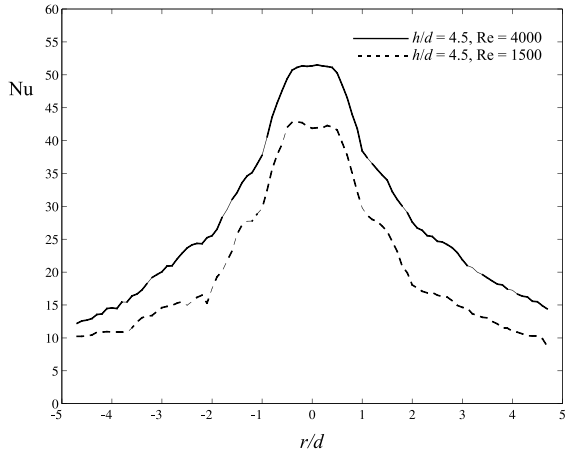

Fig. 9. Local Nu progress for configurations 3 and 4: effect of increasing Re at $h/d = 4.5$.

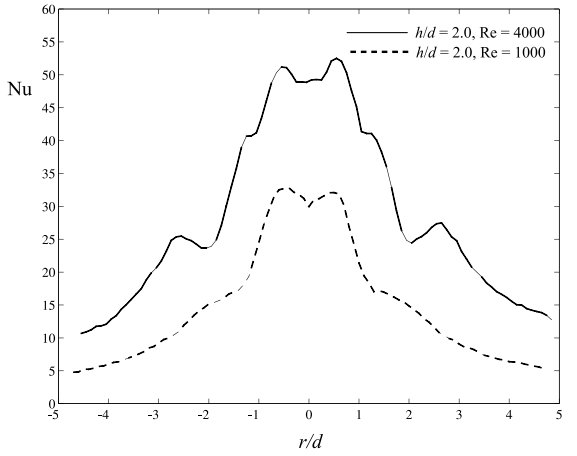

Fig. 10. Local Nu progress for configurations 1 and 2: effect of increasing Re at $h/d = 2.0$.

Furthermore, by ideally combining (superimposing) the *Nu* progress of configuration 1 in Fig. 10 with the flow field depicted in Fig. 4, one notices that the distance at which this progress is first perturbed from the bell shape ($r/d \approx 1.2$) likely corresponds to the distance from the nozzle axis at which vortices start rolling along the surface. For configuration 2 it is found: $Nu_{max} = 52.48$ at $r/d = -0.4$, $Nu_0 = 49.27$ (Table 2). For this configuration a more evident saddle-like progress is formed at stagnation: therefore to a closer jet-surface arrangement corresponds a more pronounced saddle effect, that is, a more efficient boundary layer destruction by impacting structures. Two additional secondary maxima are also noticed: these, also found in highly turbulent JI literature, are likely to be attributed to reattachment of vortical structures, as speculated by Meola et al. [22] but for much higher *Re* numbers.

For configuration 1 a complete (plane-wise) set of measurement has also been performed, to come up with the three-dimensional representation of ablation depth depicted in Fig. 11. Side lighting is provided to emphasize the relative intensity and extent of ablation depth variation, corresponding to local heat transfer along the entire impinged surface. Here saddle effect at stagnation and alteration from bell shape in the wall jet region are even more evident.

It is then instructive to compare the two local *Nu* distribution for "turbulent" configurations 2 and 4 in Fig. 12. It is seen that the departure from the bell shape (bends intensity) is largely dependent on h/d, that is, increasing for the smaller h/d value, but the overall progress (therefore the average heat transfer) depends solely on *Re*, which essentially confirms the findings by Scholtz and Trass [8] and Saad et al. [9]. Boundary layer removal by toroidal vortices is most effective for configuration 2, with its additional secondary maxima, already alluded to.

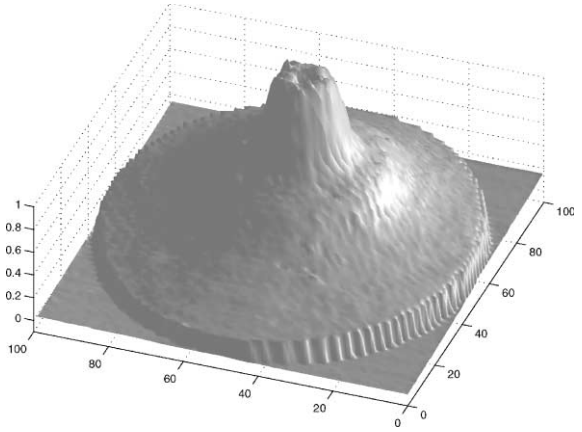

Fig. 11. 3-D representation of ablation depth for configuration 1 ($h/d = 2.0$, $Re = 1000$). Dimensions are in mm.

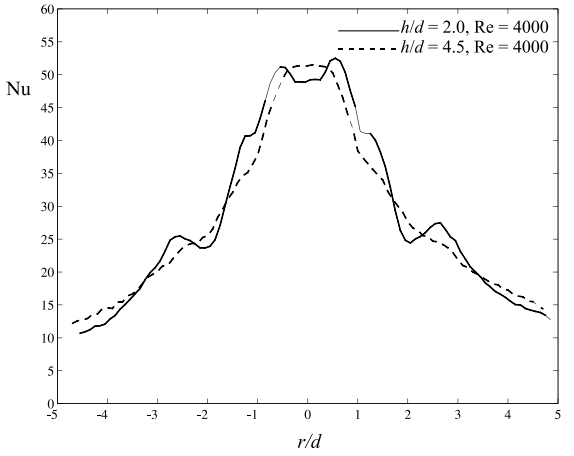

Fig. 12. Local *Nu* progress for configurations 2 and 4: effect of increasing h/d at $Re = 4000$.

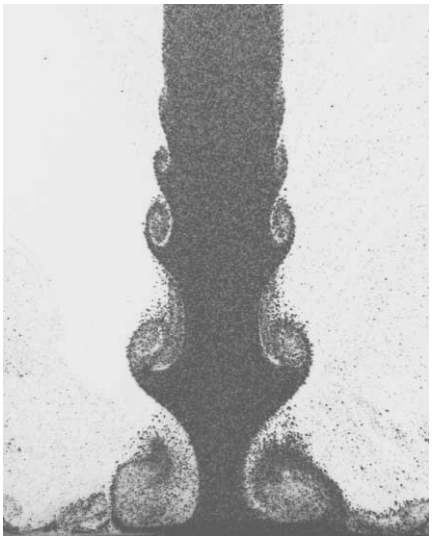

Fig. 13. Instantaneous velocity field in the stagnation and wall jet regions by PIV for $h/d = 4.5$ and $Re = 750$.

One last notation can be made with respect to the vortex frequency with which such structures impact on the plate. In Fig. 13 the visualization relative to an additional configuration ($h/d = 4.5$, $Re = 750$) is presented. Now the structures, beautifully paired, are created with a lower frequency, and boundary layer at impact location cannot be completely destroyed, therefore resulting in non-enhanced heat transfer.

3.4. Comparison with available literature data

Few references are found in the available literature, corresponding to the geometry and fluid dynamics

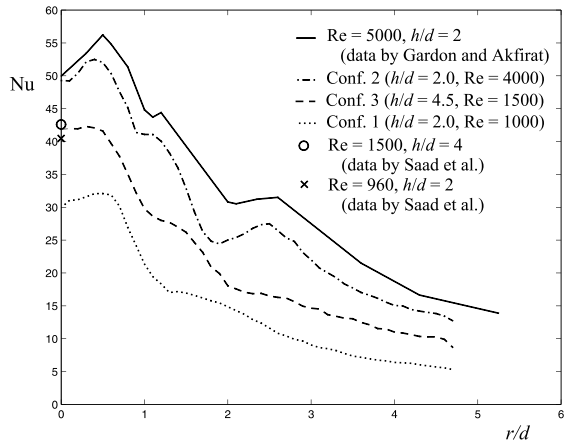

Fig. 14. Local *Nu* progress: comparison with available literature data.

arrangements adopted here, and will be briefly addressed in the following. A first comparison is provided in Fig. 14, where local heat transfer data (for $h/d = 2$ and $Re = 5000$) reported by Gardon and Akfirat [5] and stagnation data predicted by Saad et al. [9] are included. Local progress comparison with Saad et al. predictions [9] makes little sense as they used non-uniform shape jets (in a semi-confined geometry) or a flat one, but for different h/d ratio (it must be mentioned however that they failed to capture the locally non-monotone radial progress). A good agreement is found, specially with measurements by Gardon and Akfirat [5].

Another comparison is provided in Fig. 15, where local mass transfer data (for $0.5 \leqslant h/d \leqslant 6$ and $800 \leqslant Re \leqslant 970$) from [8] are included. It must be repeated that those data are referred to a non-uniform profile shape at the nozzle exit. Unexpectedly, the present heat transfer rates are consistently higher than those by Scholtz and Trass [8].

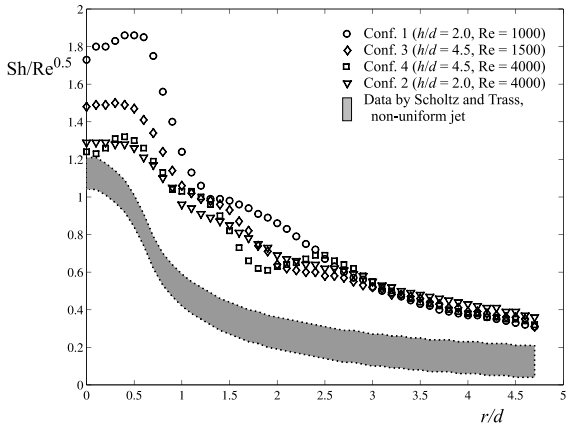

Fig. 15. Local *Nu* progress: comparison with data from Scholtz and Trass [8].

4. Conclusions

Data on radial variation of local heat transfer due to initially uniform and laminar round JI, as determined by a classical heat/mass transfer analogy, have been examined in light of an instantaneous flow visualization study, for different nozzle-to-plate spacing and fluid dynamics regimes. The non-uniformity of local heat transfer progress can be explained taking into account the influence of the coherent structures that are created at the jet interface, for their effect on boundary layer destruction upon impingement. For small nozzle-to-plate spacings a related offset of heat transfer maximum is recorded, which is comparatively larger for transitional JI. The entrainment and related pattern of structure creation is also discussed by exploiting the PIV post-processing capability, and an axial velocity pulsation is found which contributes to weaken the boundary layer stability at stagnation and affects local heat transfer.

Acknowledgements

This work was partially funded by MIUR Italian Ministry of Scientific Research, grant no. 2002093829 entitled "Aspetti fondamentali ed applicativi dei getti sommersi nelle tecniche innovative di scambio termico—Visualizzazione e simulazione integrate per la valutazione dello scambio termico da getti impingenti su piastre in configurazioni innovative".

References

[1] K. Jambunathan, E. Lai, M.A. Moss, B.L. Button, A review of heat transfer data for single circular jet impingement, Int. J. Heat Fluid Flow 13 (1992) 106–115.

[2] R. Viskanta, Heat transfer to impinging isothermal gas and flame jets, Exp. Therm. Fluid Sci. 6 (1993) 111–134.

[3] J.R. Guarino, V.P. Manno, Characterization of laminar jet impingement in portable cooling applications, in: Proceedings of the 17th Annual IEEE Semiconductor Thermal Management and Measurement Symposium, San Jose, CA, 2001, pp. 1–11.

[4] E. Elison, B.W. Webb, Local heat transfer to impinging liquid jets in the initially laminar, transitional, and turbulent regimes, Int. J. Heat Mass Transfer 37 (1994) 1207–1216.

[5] R. Gardon, J.C. Akfirat, The role of turbulence in determining the heat-transfer characteristics of impinging jets, Int. J. Heat Mass Transfer 8 (1965) 1261–1272.

[6] J.M.F. Vickers, Heat transfer coefficients between a fluid jet and normal surfaces, Ind. Eng. Chem. 51 (1959) 967–972.
[7] G.C. Huang, Investigations of heat-transfer coefficients for air flow through round jets impinging normal to a heat-transfer surface, J. Heat Transfer 85 (1963) 237–245.
[8] M.T. Scholtz, O. Trass, Mass transfer in a non-uniform impinging jet, AIChEJ 16 (1970) 82–96.
[9] N.R. Saad, W.J.M. Douglas, A.S. Mujumdar, Prediction of heat transfer under an axisymmetric laminar impinging jet, Ind. Eng. Chem. Fundam. 16 (1) (1977) 148–154.
[10] E.M. Sparrow, B.J. Lovell, Heat transfer characteristics of an obliquely impinging circular jet, J. Heat Transfer 102 (1980) 202–209.
[11] R.J. Goldstein, H.H. Cho, A review of mass transfer measurement using naphthalene sublimation, Exp. Therm. Fluid Sci. 10 (1995) 416–434.
[12] M. Angioletti, R.M. Di Tommaso, E. Nino, G. Ruocco, Local heat transfer to transitional impinging gaseous jets, in: Proceedings of the 3rd European Thermal-Science Conference, Heidelberg, vol. 2, 2000, pp. 697–700.
[13] S. Yokobori, N. Kasagi, M. Hirata, M. Nakamura, Y. Haramura, Characteristic behavior of turbulence and transport phenomena at the stagnation region of an axisymmetrical impinging jet, in: Proceedings of the 2nd International Symposium on Turbulent Shear Flows, vol. 4, 1979, pp. 12–18.
[14] C.O. Popiel, O. Trass, Visualization of a free and impinging round jet, Exp. Therm. Fluid Sci. 4 (1992) 106–115.
[15] S.L. Anderson, E.K. Longmire, Particle motion in the stagnation zone of an impinging air jet, J. Fluid Mech. 299 (1995) 333–366.
[16] J. Sakakibara, K. Hishida, M. Maeda, Vortex structure and heat transfer in the stagnation region of an impinging plane jet (simultaneous measurements of velocity and temperature fields by digital particle image velocimetry and laser-induced fluorescence), Int. J. Heat Mass Transfer 40 (1997) 3163–3176.
[17] D. Ambrose, I.J. Lawrenson, C.H.S. Sparke, The vapor pressure of naphthalene, J. Chem. Thermodyn. 7 (1975) 1173–1176.
[18] M.J. Stucky, E. Nino, B.F. Gajdeczko, P.G. Felton, Two-color particle image velocimetry technique for an internal combustion engine, Exp. Therm. Fluid Sci. 8 (1994) 305–314.
[19] M. Raffel, C. Willert, J. Kompenhans, Particle Image Velocimetry, Springer, Berlin, 1998.
[20] R. Kean, R.J. Adrian, Optimization of particle image velocimeters—Part 1. Double pulsed systems, Meas. Sci. Technol. 1 (1990) 1202–1215.
[21] U. Ullum, J.J. Schmidt, P.S. Larsen, D.R. McCluskey, Statistical analysis and accuracy of PIV data, in: Proceedings of the 2nd International Symposium on PIV, Fukui, Japan, 9–11 July 1997.
[22] C. Meola, L. deLuca, G.M. Carlomagno, Influence of shear dynamics on impingement heat transfer, Exp. Therm. Fluid Sci. 13 (1996) 29–37.